

# Arbitrary bi-dimensional finite strain cohesive crack propagation

P. Areias · D. Dias-da-Costa · J. Alfaiate · E. Júlio

Received: 29 October 2008 / Accepted: 3 September 2009 / Published online: 22 September 2009  
© Springer-Verlag 2009

**Abstract** In this paper, a systematic approach for elastic finite strain crack propagation with multiple cohesive cracks and self-contact is described. Crack paths are determined by the CTOD method and the advance criterion uses either the equivalent stress intensity factor or the tip-element stress. Crack intersections, coalescence and cohesive laws are accounted for, as is the formation of multiple particles. Globally-optimized mesh repositioning is used to minimize the least-square of all elements' inner-angle error. This is followed, in a staggered form, by a Godunov-based advection step for the deformation gradient. Several examples are presented showing the robustness and accuracy of the implementation, as well as the ability to represent crack face thickness variation in finite strains. Classical fracture benchmarks are solved and a problem of multiple crack evolution is proposed. Excellent results were observed in the effected tests.

**Keywords** Fracture · Arbitrary Lagrangian–Eulerian method · Cohesive cracks · Nonlinear elasticity

P. Areias (✉) · J. Alfaiate  
ICIST, Instituto de Engenharia de Estruturas,  
Território e Construção, Lisbon, Portugal  
e-mail: pareias@civil.ist.utl.pt  
URL: www.home.uevora.pt/~pmaa/

D. Dias-da-Costa · E. Júlio  
ISISE, Departamento de Engenharia Civil,  
Universidade de Coimbra, Lisbon, Portugal  
e-mail: dcosta@dec.uc.pt

E. Júlio  
e-mail: ejulio@dec.uc.pt

J. Alfaiate  
DECIVIL, Departamento de Engenharia Civil,  
IST, Instituto Superior Técnico, Universidade Técnica de Lisboa,  
Lisbon, Portugal  
e-mail: alfaiate@civil.ist.utl.pt

## 1 Introduction

Bi-dimensional crack propagation algorithms have been developed in the past two decades with varying degrees of effectiveness and generality. Existing techniques can be classified as discrete or continuum-based:

- Full and local remeshing procedures [12, 16], numerous local displacement [26, 28, 31, 32] (or strain [2, 35]) enrichments, clique overlaps [24], edges repositioning or edge-based fracture with R-adaptivity [30];
- Element erosion [41], smeared band procedures [34], viscous-regularized techniques [21], gradient and non-local continua [40].

In the context of finite strain simulation, each one has specific advantages which we weighed before taking the decision documented in this paper. In particular, the extended finite element method (XFEM) by Belytschko and co-workers [11, 32] was used previously but still poses challenges for large amplitude displacements and also multiple intersections. Concerning the latter, densification of the Jacobian matrix occurs due to pile-up of degrees-of-freedom for nodes contributing to multiple cracks. If  $n_c$  cracks are present in elements in the support of a given node, this has  $(1 + n_c)n_{SD}$  degrees of freedom where  $n_{SD}$  is the number of spatial dimensions; this produces a fill-in the sparse Jacobian contrasting with remeshing that retains sparsity along the analysis (by increasing the number of nodes). Large displacements with contact or cohesive forces between crack faces are directly dealt with classical computational geometry search and collision detection algorithms. The adaptation of these to deal with enriched elements is of debatable scientific value. However, it is noticeable that large amplitude displacements are perfectly managed (see, e.g. [27]) by

XFEM if neither contact nor cohesive forces are present. A noticeable development of XFEM for large displacements is the one of Legrain and co-workers [27].

Both difficulties can be mitigated at the cost of intricate coding. As a consequence of these difficulties, typically idealized numerical examples are displayed. Features are then added, such as crack face friction, coupled heat transfer, etc., which share the inherited limitations of the maiden work. Here, the opposite direction is taken: we start with a general fracturing approach, valid for finite strains and multiple cracks, which is then particularized for specific problems.

From the enumerated options, it is often pointed out that local remeshing techniques lead to ill-formed elements (in particular blade and dagger-shaped triangles) which compromise the solution accuracy. These ill-formed elements motivate, besides other aspects, the use of full remeshing. However, mesh-generation groups have developed high-performance node-reposition (smoothing) methods perfectly capable of removing severe ill-formations (see, e.g. [43]). Therefore, a combination of local remeshing and node-repositioning is proposed here. Specifically, a staggered approach (constrained analysis, detection, recursive local remeshing, node repositioning, advection) is introduced. Crack advance occurs when either the equivalent stress intensity factor exceeds the maximum allowed value for linear elastic fracture mechanics (LEFM) or when the maximum principal stress  $\sigma_1$  ahead of the crack tip exceeds the critical material stress  $f_t$ . Crack trajectories stem from stress intensity factors calculated from the crack tip opening displacement (CTOD) criterion in both cases, following well-known relations. The node repositioning uses a (global) non-linear least-square finite element method (LSFEM) which minimizes the norm of the sum of element internal angles to reposition the reference nodes. This always results in well-formed elements avoiding crack path inaccuracies and spurious arrests due to the crack turning back.

This paper is organized as follows: Sect. 2 presents the kinematics, constitutive laws and cohesive formulation; Sect. 3 describes the propagation algorithm (advance and global minimization methods); six numerical examples (including two newly proposed) are presented in Sect. 4 and explored to obtain a clear picture of the expected performance and possible problems. Finally, concluding remarks appear in Sect. 5.

## 2 Governing equations

### 2.1 Kinematics, equilibrium and material model

The crack propagation problem can be decomposed into a classical continuum mechanics step and a sequence of remeshing and node reposition steps, followed by an advection

step. Conventional continuum mechanics notation is adopted (e.g. [3]) and derivations are mostly standard. Equilibrium is established using the displacement-based virtual work principle. The open set  $\Omega_0 \subset \mathbb{R}^3$  is the material configuration of a given body whose external boundary includes pre-existing cracks and notches. It is assumed that each point  $X$  is associated by a bijective map to its position in that configuration:  $X \rightarrow \mathbf{X} \in \Omega_0$ . To contrast with the material configuration, lower-case letters are used for quantities defined in the deformed configuration. In this sense  $\mathbf{x}$  is the spatial position; additionally, we assume that there exists a function (to spare the notation we overload the symbols)  $\mathbf{x} \equiv \mathbf{x}(\mathbf{X})$ . The difference between positions, with  $X$  fixed, is the displacement,  $\mathbf{u}(X) = \mathbf{x}[\mathbf{X}(X)] - \mathbf{X}(X)$ . All measures of deformation in  $\Omega_0$  stem from the deformation gradient,  $\mathbf{F} = \frac{\partial \mathbf{x}}{\partial \mathbf{X}}$ . Energy conjugacy with  $\mathbf{F}$  requires a counterpart stress quantity, which we denote as the first Piola–Kirchhoff stress  $\mathbf{P}$ . Essential and natural boundary conditions (corresponding to domains  $\Gamma_{\bar{\mathbf{u}}}$  and  $\Gamma_{\bar{\mathbf{t}}}$ , respectively, such as  $\Gamma = \Gamma_{\bar{\mathbf{u}}} \cup \Gamma_{\bar{\mathbf{t}}}$ ,  $\Gamma_{\bar{\mathbf{u}}} \cap \Gamma_{\bar{\mathbf{t}}} = \emptyset$ ) are also required ingredients. In addition, there exists a vector-valued function of body forces  $\mathbf{B}$ .

The equilibrium equations and boundary conditions in the strong form are stated as:

$$\nabla_0 \cdot \mathbf{P}^T + \mathbf{B} = \mathbf{0} \quad \text{in } \Omega_0 \quad (1)$$

$$\mathbf{u} = \bar{\mathbf{u}} \quad \text{on } \Gamma_{\bar{\mathbf{u}}} \quad (2)$$

$$\mathbf{t} = \bar{\mathbf{t}} \quad \text{on } \Gamma_{\bar{\mathbf{t}}} \setminus \Gamma_{\sigma_n} \quad (3)$$

$$\mathbf{t} \cdot \mathbf{n} = \sigma_n([[\mathbf{u}]]_n) \quad \text{on } \Gamma_{\sigma_n} \quad (4)$$

Note that, by use of the Dirac-delta distribution, we can write  $\bar{\mathbf{t}} = \delta_{\Gamma_{\bar{\mathbf{t}}}} \mathbf{B}$  with  $\delta_{\Gamma_{\bar{\mathbf{t}}}} = 0$  a.e. in  $\Omega_0$  and  $\delta_{\Gamma_{\bar{\mathbf{t}}}} = +\infty$  in  $\Gamma_{\bar{\mathbf{t}}}$ . Also, in part of  $\Gamma_{\bar{\mathbf{t}}}$  ( $\Gamma_{\sigma_n}$ ), a specific stress is imposed: the cohesive crack stress  $\sigma_n$ , is assumed to depend on  $[[\mathbf{u}]]_n$ , the crack opening. The symbol  $\nabla_0$  means gradient with respect to  $\mathbf{X}$ . Also shown in Fig. 1 is the boundary  $\Gamma_{\bar{\mathbf{X}}}$  (which coincides with the complete boundary  $\Gamma$ ), meaning that: the body is completely defined by  $\Gamma$  and therefore original point coordinates in this boundary must remain there. Later in the text we will introduce a reference system whose boundary coincides with the material one. Use of standard arguments in continuum mechanics results in the following weak form of equilibrium:

$$\begin{aligned} \delta W = & \int_{\Omega_0} (\boldsymbol{\tau} : \nabla \mathbf{u}^\Delta - \mathbf{B} \cdot \mathbf{u}^\Delta) d\Omega_0 - \int_{\Gamma_{\bar{\mathbf{t}}} \setminus \Gamma_{\sigma_n}} \bar{\mathbf{t}} \cdot \mathbf{u}^\Delta d\Gamma_{\bar{\mathbf{t}}} \\ & - \int_{\Gamma_{\sigma_n}} \sigma_n[[\mathbf{u}]]_n^\Delta d\Gamma_{\sigma_n} \equiv 0 \end{aligned} \quad (5)$$

where  $\nabla \bullet = \nabla_0 \bullet \mathbf{F}^{-1}$  and  $\boldsymbol{\tau} = \mathbf{P} \mathbf{F}^T$  is the Kirchhoff stress. The symbol  $\Delta$  represents the change in the affected kinematic quantity; this means that  $\mathbf{u}^\Delta$  satisfies homogeneously the essential boundary conditions (the notation is also used by

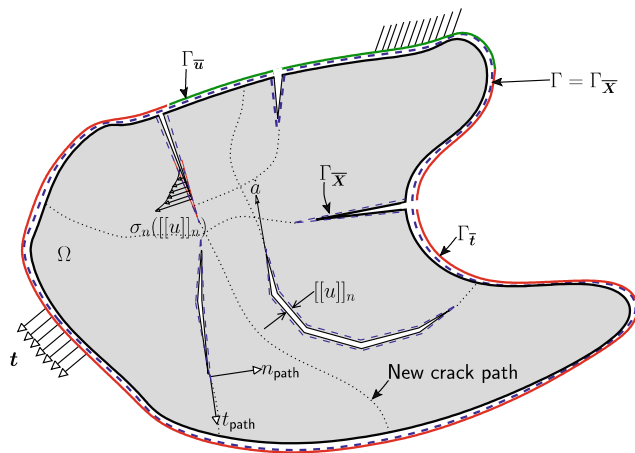


**Fig. 1** Multiple fracturing non-linear continuum: boundaries, loading and normal jump definition

Antman [3]). Solutions of (5) include solutions of the equilibrium system. Minimization of the work function could have been adopted, but since complementarity may be present in the cohesive term, that work function is not differentiable in the classical sense. The first variation of (5) is required for use in the Newton–Raphson method and is given by:

$$\begin{aligned} \Delta \delta W = & \int_{\Omega_0} \left[ \nabla \mathbf{u}^\Delta : \mathbf{c} : \nabla \Delta \mathbf{u} - \Delta \mathbf{B} \cdot \mathbf{u}^\Delta \right. \\ & + \boldsymbol{\tau} : \left( \nabla \Delta \mathbf{u}^T \nabla \mathbf{u}^\Delta \right) \Big] d\Omega_0 - \int_{\Gamma_t \setminus \Gamma_{\sigma_n}} \Delta \bar{\mathbf{t}} \cdot \mathbf{u}^\Delta d\Gamma_t \\ & - \int_{\Gamma_{\sigma_n}} \left( \Delta \sigma_n [[\mathbf{u}]]_n^\Delta + \sigma_n \Delta [[\mathbf{u}]]_n^\Delta \right) d\Gamma_{\sigma_n} \end{aligned} \quad (6)$$

where  $\Delta \bullet$  indicates an infinitesimal change in  $\bullet$ . We use the compressible neo-Hookean hyperelastic law, whose strain energy function is given by (see [14, eqs. 5.28 and 5.29]):

$$\psi = \frac{\mu}{2} (I_b - 3) - \mu \ln J + \frac{\lambda}{2} (\ln J)^2 \quad (7)$$

with  $J = \det \mathbf{F}$  and  $I_b = \text{tr}[\mathbf{F} \mathbf{F}^T]$ . Properties  $\mu$  and  $\lambda$  are extensions of the small-strain shear modulus and Lamé’s parameter, respectively. For the compressible neo-Hookean material with Lamé parameters  $\mu$  and  $\lambda$ , the Kirchhoff stress and modulus are respectively given by:

$$\boldsymbol{\tau} = \mu (\mathbf{F} \mathbf{F}^T - \mathbf{I}) + \lambda \ln\{\det[\mathbf{F}]\} \mathbf{I} \quad (8)$$

$$\mathbf{c} = \lambda \mathbf{I} \otimes \mathbf{I} + (\mu - \lambda \ln\{\det[\mathbf{F}]\}) \mathcal{I} \quad (9)$$

where  $\mathbf{I}$  is the second-order identity tensor and  $\mathcal{I}$  is the fourth-order symmetric identity tensor. The surface cohesive law, returning  $\sigma_n$ , is given in Sect. 2.4. Although arbitrary Lagrangian–Eulerian (ALE) techniques are often introduced at the continuum level (e.g. [9]), this requires some level of complexity that we avoid here.

## 2.2 Kinematic discrete form

Standard finite-element notation is used: parent-domain coordinates are  $\theta^1$  and  $\theta^2$  and  $X_i^K$  is the  $i$ th coordinate of local node  $K$  (as well as  $u_i^K$  for the corresponding displacement). Remeshing methods make use of an intermediate set of nodal coordinates, between the spatial  $x_i^K$  and the material  $X_i^K$ , which we denote by reference coordinates,  $\chi_i^K$ . Using the chain-rule we can calculate the deformation gradient as:

$$\mathbf{F} = \mathbf{f} \mathbf{F}_o \quad (10)$$

where  $\mathbf{F}_o = \frac{\partial \mathbf{x}}{\partial \mathbf{X}}$  and  $\mathbf{f} = \frac{\partial \mathbf{x}}{\partial \boldsymbol{\chi}}$ . The deformation gradient  $\mathbf{F}_o$  becomes a history variable, to be re-mapped by an advection step (see Sect. 3.3). Since (10) affects the Jacobian, an analogous relation for  $\mathbf{J}$  is obtained:

$$\mathbf{J} = j \mathbf{J}_o \quad (11)$$

$$\mathbf{u} = \begin{Bmatrix} (1 - \theta^1 - \theta^2) u_1^1 + \theta^1 u_1^2 + \theta^2 u_1^3 \\ (1 - \theta^1 - \theta^2) u_2^1 + \theta^1 u_2^2 + \theta^2 u_2^3 \end{Bmatrix} \quad (12)$$

$$j = \chi_2^3 \chi_1^2 + \chi_1^1 \chi_2^2 + \chi_2^1 \chi_1^3 - \chi_2^1 \chi_1^2 - \chi_2^2 \chi_1^3 - \chi_1^1 \chi_2^3 \quad (13)$$

$$\mathbf{f} = \frac{1}{j} \cdot \begin{bmatrix} j + (u_1^3 - u_1^1)(\chi_2^1 - \chi_2^2) + (u_1^2 - u_1^1)(\chi_2^3 - \chi_2^1) \\ (u_2^3 - u_2^1)(\chi_2^1 - \chi_2^2) + (u_2^2 - u_2^1)(\chi_2^3 - \chi_2^1) \\ (u_1^3 - u_1^1)(\chi_1^2 - \chi_1^1) + (u_1^2 - u_1^1)(\chi_1^3 - \chi_1^1) \\ (u_2^3 - u_2^1)(\chi_1^2 - \chi_1^1) + (u_2^2 - u_2^1)(\chi_1^3 - \chi_1^1) \end{bmatrix} \quad (14)$$

Remaining quantities can be directly obtained from these, and therefore are omitted. This simplicity allows a very fast computation and stable residual behavior. These aspects are far more important for rough problems (like fracture) than for pure convergence rate of the results. In addition, convergence rate is limited by the equilibrium equation regularity [25], and therefore higher-order elements are inappropriate for this application.

## 2.3 Cohesive discretization

The representation of the finite-displacement cohesive element makes use of a five node arrangement as depicted in Fig. 2. This is an extension, with two additional nodes, of the classical point-to-segment contact element, here with a cohesive law. We consider all external edges (i.e. with only one underlying solid element) and perform a two-pass enforcement. Certain geometrical aspects are dealt with in Chapter 23 of the book by Crisfield [17], although we used Mathematica [42] with the Acegen add-on to obtain the relevant code.

## 2.4 Mixed-mode traction separation law

We use a damage-based elastic traction-separation law dependent on three constitutive properties,  $f_t$ ,  $G_F$  and  $\beta$  which are

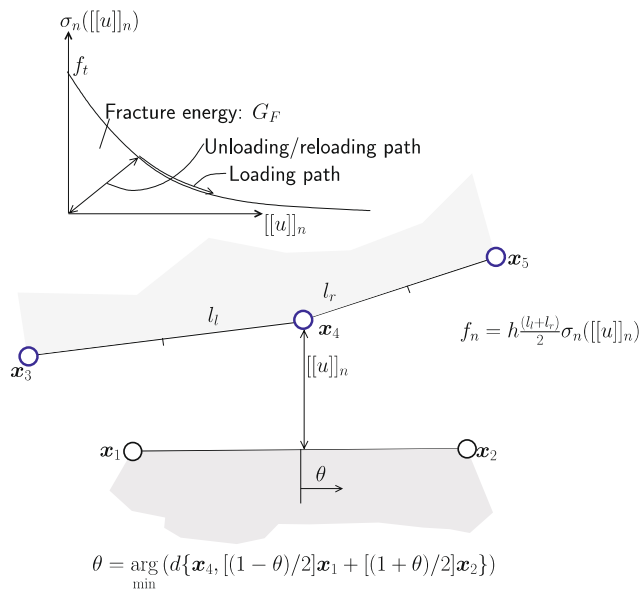


**Fig. 2** Five node cohesive element for finite displacements;  $h$  represents the thickness

the tensile strength, the fracture energy and a mode II parameter, respectively. It is an adaptation of the law proposed by Alfaiate et al. [1] to deal with unloadings/reloadings with negative  $w_n$ . It incorporates the closure effect, mode II damaging effect and unloading to origin. A thorough discussion of cohesive representations is provided in the paper by Elices et al. [19]. The damage variable is denoted as  $d$ ; normal and tangential stresses are denoted as  $\sigma$  and  $\tau$ , respectively, and are grouped in a traction vector  $\mathbf{t}$  which is given using the  $1-d$  pre-multiplication:

$$\mathbf{t} = \begin{Bmatrix} \sigma \\ \tau \end{Bmatrix} = (1-d) \frac{f^*}{\kappa_0} \begin{Bmatrix} a w_n \\ w_t \end{Bmatrix} \quad (15)$$

where  $w_n$  is the normal displacement,  $w_t$  is the tangential displacement and  $a$  is the crack closure parameter;  $f^*$  and  $\kappa_0$  are the initial stress and the kinematical shift, respectively. The damage parameter depends on a kinematical variable,  $\kappa$ , according to the following rate law:

$$\dot{d} = e^{-\frac{f_t}{G_F}(\kappa)} \left\{ \frac{\kappa_0 [G_F + f_t \kappa]}{G_F \kappa^2} \right\} \dot{\kappa} \quad (16)$$

where  $\kappa_0$ , the kinematical shift, is introduced to avoid the initial infinite slope. The kinematical variable  $\kappa$  can be viewed as the “equivalent opening”, a quantity to be defined by complementarity conditions. We use a non-dimensional tolerance,  $\text{tol}$ , to define  $\kappa_0$ :

$$\kappa_0 = 2\text{tol} \frac{G_F}{f_t} \quad (17)$$

The crack closure parameter is a function of the opening sign:

$$a = \begin{cases} 1, & w_n \geq 0 \\ \frac{1}{1-d}, & w_n < 0 \end{cases} \quad (18)$$

this allows a fixed slope for contact and keeps the tangential stress unaltered in penetration. The initial stress is obtained after replacement of the kinematical shift in the damage expression:

$$f^* = [1 - d(\kappa = 0)] f_t \quad (19)$$

The evolution of  $\kappa$  is implicitly defined by the following complementarity conditions:

$$\begin{aligned} \dot{d} &\geq 0 \\ \dot{\phi} &= 0 \\ \phi &\leq 0 \end{aligned} \quad (20)$$

with the fracture surface being defined by the level sets of the following function (of  $w_n$  and  $w_t$ ):

$$\phi = \langle w_n \rangle + \beta |w_t| - \kappa \quad (21)$$

This simple mixed-mode law and the related kinematical shift were found to be sufficient for the examples under study, although complete solutions to this class of problems resort to the concept of set-valued forces [7, 22].

### 3 Crack propagation algorithm

Our crack propagation algorithm is a sequence of five steps:

1. Satisfaction of the advance criterion
2. Tip edge insertion
3. Global minimization mesh smoothing
4. Godunov advection step
5. Solution with constrained tip.

Brief descriptions are given in the following sub-sections. Note that simultaneous crack growth and multiple-edge growth is possible, as are intersections and coalescence.

#### 3.1 Advance criterion

According to the case (LEFM critical equivalent stress intensity factor and cohesive fracture) one of the following fracture criteria is used:

- LEFM: critical equivalent stress intensity factor  $K_{eq} > K_{lc}$ .
- Cohesive fracture: critical principal stress ahead of the crack tip  $\sigma_1 > f_t$ .

The use of LEFM in finite strain problems requires the assumption of sufficiently small strains near the process zone. Fracture of polymers often makes use of LEFM despite the presence of large strains away from the tips.

The equivalent stress intensity factor is given, after direct manipulation (see the treatise by Bažant and Planas [10]):

$$K_{eq} = \frac{E}{4} \sqrt{\frac{\pi}{2R}} \sqrt{d_I^2 + d_{II}^2} \quad (22)$$

where  $E$  is the elasticity modulus and  $R$  is given by (see Fig. 3):

$$R = \frac{1}{2} \|\mathbf{x}_{N_D} - \mathbf{x}_{N_T}\|_2 + \frac{1}{2} \|\mathbf{x}_{N_O} - \mathbf{x}_{N_T}\|_2 \quad (23)$$

We use the displacement field to estimate  $K_{eq}$ . The mode II vector is given by:

$$\mathbf{v}_{II} = \mathbf{x}_{N_T} - (\mathbf{x}_{N_D} + \mathbf{x}_{N_O})/2 \quad (24)$$

and the mode I vector is given by:  $\mathbf{v}_I = \mathbf{e}_3 \times \mathbf{v}_{II}$  with  $\mathbf{e}_3 = \{0, 0, 1\}^T$ .

The difference in near-tip displacement is given by:

$$\Delta \mathbf{u}_T = \mathbf{u}_{N_D} - \mathbf{u}_{N_O} \quad (25)$$

from which the mode I and II displacements are given by projection:

$$d_I = \Delta \mathbf{u}_T \cdot \hat{\mathbf{v}}_I \quad (26)$$

$$d_{II} = \Delta \mathbf{u}_T \cdot \hat{\mathbf{v}}_{II} \quad (27)$$

where the notation  $\hat{\bullet} = \bullet / \|\bullet\|_2$  was used. For cohesive fracture, the tip is constrained by a penalty to be closed and, if the resulting stress is greater than  $f_t$ , the tip is released.

### 3.2 Tip edge insertion

In the discrete setting, the tip advance (an incremental length  $\Delta a$ ) corresponds exactly to a newly introduced edge, whose origin is the previous tip and the destination is the new tip, which is a convex combination of the opposing edge nodes (see Fig. 3). The algorithm is the following sequence:

1. Search for candidate outer edges and respective  $T$ ,  $O$  and  $N$  nodes (see Fig. 3i)
2. For each candidate edge pair, determine either the tip normal stress or the CTOA
3. Sort the candidates according to the critical values
4. Calculate the crack direction using the CTOD (28, 29) and check for advance
5. Based on the crack direction, calculate the affected element and the corresponding intersection with the opposite edge. This involves the identification of  $D$  and  $O$  edges (in Fig. 3ii). If there is a neighborhood element then split it by joining with the opposite node. The total

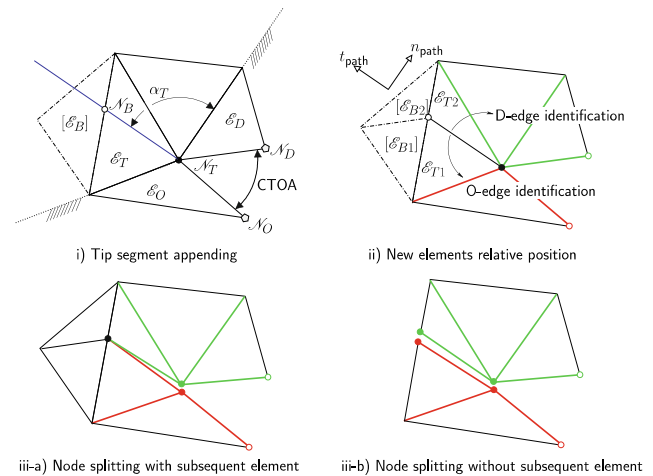


**Fig. 3** 2D crack advance with minimal remeshing

splitting will result in elements  $\mathcal{E}_{T1}$ ,  $\mathcal{E}_{T2}$  and, if the element ahead of the tip exists,  $\mathcal{E}_{B1}$  and  $\mathcal{E}_{B2}$ . The connectivities are obtained by application of modulus algebra, resulting in a very concise code.

The crack path orientation (the orientation of the new edge) in pure mode I is given by:

$$\mathbf{v}_{PATH} = \hat{\mathbf{v}}_I \sin(\theta_c) + \hat{\mathbf{v}}_{II} \cos(\theta_c) \quad (28)$$

where  $\theta_c$ , in degrees, is given by:

$$\theta_c = -36.5 \arctan \left[ 2.2 \arctan \left( \frac{d_{II}}{d_I} \right) \right] \quad (29)$$

This is the criterion of Ma and Sutton [29] for LEFM. Despite the simplicity of the above criterion, surprisingly accurate crack paths are obtained. This contrasts with the Rankine criterion [19] since the FE displacements are much more accurate than stresses; despite this fact, mesh quality has a very important effect in the crack path results. Therefore, we use a global node repositioning minimization algorithm to ensure mesh quality along the propagation process.

### 3.3 Element-based global minimization smoothing and advection

The mesh repositioning algorithm makes use of a least-square finite element procedure for the minimization of the inner angle differences with  $\pi/3$ . The problem consists of a minimization of a potential which is a function of the *reference* coordinates. Each smoothing-element provides a local gradient and a Hessian matrix of its least-square contribution. The quantity to be minimized is the following sum over the



number of elements ( $n_e$ ) and the number of local nodes (3):

$$\Pi_{\text{angle}} = \frac{1}{2} \sum_{e=1}^{n_e} \sum_{i_e=1}^3 (\Delta\alpha_{i_e}^e)^2 \quad (30)$$

where

$$\Delta\alpha_{i_e}^e = s \arctan \left( \frac{\|\mathbf{a}_{i_e} \times \mathbf{b}_{i_e}\|}{|\mathbf{a}_{i_e} \cdot \mathbf{b}_{i_e}|} \right) - \frac{\pi}{3} \quad (31)$$

with  $s = \text{sign}[\mathbf{e}_3 \cdot (\mathbf{a}_{i_e} \times \mathbf{b}_{i_e})]$ . The vectors  $\mathbf{a}_{i_e}$  and  $\mathbf{b}_{i_e}$  depend on the nodal coordinates according to the usual notation of modulus algebra:

$$\mathbf{a}_{i_e} = \mathbf{x}_{i_e+1_3} - \mathbf{x}_{i_e} \quad (32)$$

$$\mathbf{b}_{i_e} = \mathbf{x}_{i_e+2_3} - \mathbf{x}_{i_e} \quad (33)$$

To monitor the mesh quality (in degrees), the measured angle error is introduced by the following formula:

$$\varepsilon_\alpha = \frac{27.0095 \sqrt{\Pi_{\text{angle}}}}{n_e} \quad (34)$$

where convergence to degrees and nodal average were effected. Grouping all nodal positions as generalized coordinates  $\mathbf{x}_v = \{\chi_{11}, \chi_{12}, \dots, \chi_{\text{nnol}}, \chi_{\text{nnol}2}\}$ , we obtain the corresponding internal force and stiffness of the “angle-element” set from the first and second derivatives of  $\Pi_{\text{angle}}$ :

$$\mathbf{f}^\alpha = \frac{\partial \Pi_{\text{angle}}}{\partial \mathbf{x}_v} \quad (35)$$

$$\mathbf{K}^\alpha = \frac{\partial^2 \Pi_{\text{angle}}}{\partial \mathbf{x}_v \partial \mathbf{x}_v} \quad (36)$$

The solution of  $\mathbf{f}^\alpha(\mathbf{x}_v) = 0$  with  $\Delta\mathbf{x}_{\text{ino}} = \mathbf{0}$  if  $\text{ino} \in \Gamma$  provides the repositioned set  $\mathbf{x}_v$  minimizing  $\Pi_{\text{angle}}$ .

The advection process follows the first-order Godunov scheme (e.g. [9,37,38]) which we specify here for our triangle mesh arrangement. A comprehensive description of this scheme is given in the LS-DYNA theory manual [23], Chapter 17. In particular, we use their full-donor approximation. Figure 4 shows the quantities participating in the advection scheme for each triangular element. In 1D, the field transference corresponds to the motion of a node inside a line segment, and hence can be accounted exactly. In 2D, we are left with a set of established practices to choose from. The Godunov scheme was developed elsewhere and hence is only sketched here.

The corrected deformation gradient  $\mathbf{F}_o^e$ , as a history variable in element  $e$ , is obtained after a smoothing step as:

$$\mathbf{F}_o^e = \mathbf{F}^e + \frac{1}{2A_e} \sum_{L=1}^3 \left\{ \left[ l_L \mathbf{n}_L \cdot (\Delta\mathbf{x}_{\overline{L}_3} + \Delta\mathbf{x}_{\overline{L+1}_3} - \Delta\mathbf{x}_{\overline{L}_3} - \Delta\mathbf{x}_{\overline{L+1}_3}) \right] (\mathbf{F}^{e(L)} - \mathbf{F}^e) \right\} \quad (37)$$

where modulus algebra was employed. Please compare this equation with Eq. (26) of reference [37]. Equation (37) is a

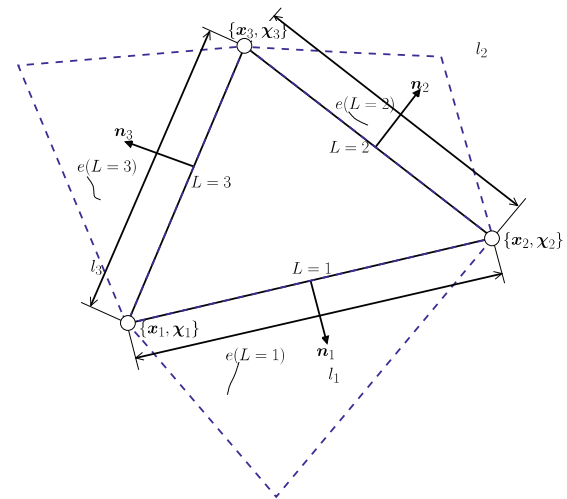


Fig. 4 Relevant quantities involved in the ALE Godunov scheme

specialization for the three-node triangle by rearrangement of Eq. (26) of [37]. The elements represented with a dashed line in Fig. 4 are neighborhood elements providing  $\mathbf{F}^{e(L)}$ . Note that the plus function is given by  $(\bullet)_+ = \max(0, \bullet)$  and is introduced to impose the direction of flow. The well known drawback of this approach, which is the restriction to piecewise constant fields, is of no consequence in our work, since constant- $\mathbf{F}$  elements are used. The simplicity of this approach stems from the absence of spatial derivatives, required in other methods.

### 3.4 Solution with linear arc-length constraint and multipoint constraints

In the determination of the load (or displacement) factor, which we denote here as  $\lambda$ , either the equivalent stress intensity factor ( $K_{\text{eq}}$ ) or the stress is constrained. A discussion of the constraint is given in Moës and Belytschko [31]. However, in that paper the Authors avoided a full consistent linearization for the constraint equation, performed here.

If a load-parameter  $\lambda$  is included as an unknown, the system must be enlarged by appending a new equation  $s(\mathbf{u}) = 0$ :

$$\mathbf{r}(\lambda, \mathbf{u}) = \mathbf{0} \quad (38)$$

$$s(\mathbf{u}) = 0 \quad (39)$$

where  $\mathbf{r}(\lambda, \mathbf{u})$  is the discrete equilibrium residual and  $s(\mathbf{u})$  is the crack constraint. The solution by Newton–Raphson iteration ( $i_t$  is the iteration counter) results in:

$$\begin{bmatrix} \mathbf{K}(\lambda_{i_t}, \mathbf{u}_{i_t}) & -\mathbf{e}(\lambda_{i_t}, \mathbf{u}_{i_t}) \\ -\frac{ds(\mathbf{u}_{i_t})}{d\mathbf{u}} & 0 \end{bmatrix} \begin{bmatrix} \mathbf{u}_v \\ \lambda_v \end{bmatrix} = \begin{bmatrix} \mathbf{r}(\lambda_{i_t}, \mathbf{u}_{i_t}) \\ s(\mathbf{u}_{i_t}) \end{bmatrix} \quad (40)$$

where  $\mathbf{u}_v = \mathbf{u}_{i_t+1} - \mathbf{u}_{i_t}$  and  $\lambda_v = \lambda_{i_t+1} - \lambda_{i_t}$ . Omitting the iteration counter  $i_t$ ,

$$\mathbf{e}(\lambda, \mathbf{u}) = \frac{\partial \mathbf{r}(\lambda, \mathbf{u})}{\partial \lambda} \quad (41)$$

$$\mathbf{K}(\lambda, \mathbf{u}) = -\frac{\partial \mathbf{r}(\lambda, \mathbf{u})}{\partial \mathbf{u}} \quad (42)$$

Defining  $\mathbf{u}_r = \mathbf{K}^{-1} \mathbf{r}$  and  $\mathbf{u}_e = \mathbf{K}^{-1} \mathbf{e}$ , and  $s_r = \frac{ds}{du} \mathbf{u}_r$ ,  $s_e = \frac{ds}{du} \mathbf{u}_e$  we obtain:

$$\lambda_v = \frac{-s_r(\mathbf{u}_{i_t}) - s(\lambda, \mathbf{u}_{i_t})}{s_e(\lambda, \mathbf{u}_{i_t})} \quad (43)$$

$$\mathbf{u}_v = \mathbf{u}_r + \mathbf{u}_e \lambda_v \quad (44)$$

which provides the overall solution process for the constrained equilibrium. If several cracks are present, the constraint is applied to the one presenting the largest  $K_{eq}$ .

The imposition of multipoint constraints in the code (see [4]) uses clique operations and is based on the additional imposition of the equality  $\mathbf{t}(\mathbf{u}) = \mathbf{0}$  where  $\mathbf{t}$  is a vector with  $m$  components. If  $m$  unknowns to retain are selected, we can apply Newton's method and solve for  $\mathbf{u}_m$  as a function of the remaining  $n - m$  unknowns ( $n$  is the number of the unconstrained degrees of freedom). We use the subscript  $s$  for the dependent unknowns:

$$\mathbf{u}_{vs} = -\left(\frac{\partial \mathbf{t}}{\partial \mathbf{u}_s}\right)^{-1} \left(\frac{\partial \mathbf{t}}{\partial \mathbf{u}_m}\right) \mathbf{u}_{vm} - \left(\frac{\partial \mathbf{t}}{\partial \mathbf{u}_s}\right)^{-1} \mathbf{t} \quad (45)$$

Enlarging (45) to include all unknowns in the left-hand-side, and rearranging the Jacobians in transformation matrices, we obtain

$$\mathbf{u}_{vs} = \mathbf{T} \mathbf{u}_{vm} + \mathbf{b} \quad (46)$$

which, inserted in the equilibrium system and pre-multiplying by  $\mathbf{T}^T$ , provides

$$\mathbf{T}^T \mathbf{K} \mathbf{T} \mathbf{u}_s = \mathbf{T}^T \mathbf{r} - \mathbf{T}^T \mathbf{K} \mathbf{b} \quad (47)$$

The  $n - m$  unknowns in the reduced system satisfy (tangentially) the constraints. This is used to force certain symmetries and anti-symmetries and to force a set of nodes to have the same displacement, etc.

## 4 Numerical examples

Six numerical examples are tested with the code SIMPLAS [4], created by the first Author and used previously in a variety of problems. The examples show exceptional robustness for the crack path and very good agreement with the experimental results; both LEFM (cohesionless) and cohesive cracks are analyzed and comparisons are made with both experimental and alternative numerical results from other

Authors. Combined use of multipoint constraints and continuation methods is made to avoid crack tip retention and to control the opening.

### 4.1 Study of thickness variation in pulling test

In this test, we use the zero out-of-plane normal stress condition to obtain the thickness variation in a plate with a central crack. Classical fracture mechanics are used to propagate the crack. The  $K_I$  stress intensity factor is used as control variable. Three values of  $G_F \in \{\frac{1}{2}, 5, 20\}$  consistent units are tested with two initial meshes (4,678 and 19,278 elements). Crack-advance is imposed in each time step before a full crack is developed and the most critical crack tip is used to enforce the strain energy release rate. The relevant data is shown in Fig. 5. Thickness contour plots for  $G_F = 20$  are shown in Fig. 6 using the true deformed geometry of the specimen and Fig. 7 shows the evolution of  $P$  and  $\bar{u}$  with the crack length. Despite the absence of cohesive law (dissipation occurs at the tips) relatively mesh-invariant results are obtained.

### 4.2 Bittencourt's drilled plate

To evaluate the crack path accuracy of the proposed technique, we use the example by Bittencourt et al. [12] who studied curvilinear crack propagation both experimentally and numerically. Specimens are made of polymethylmethacrylate (PMMA) and large deformations are present. The geometry, material properties and boundary conditions are depicted in Fig. 8 for two specimens differing in the dimensions  $a$  and  $b$ . In reference [12], the Erdogan-Sih [20] (this was found to be the most accurate) fracture criterion was used, with stress intensity factors calculated in a variety of forms, including the domain-integral (see also [31] for a more recent application) and quarter-point elements. In that paper, a recursive spatial decomposition method was introduced to subdivide the mesh. Specially refined elements were used in the neighborhood of the holes and the Authors have

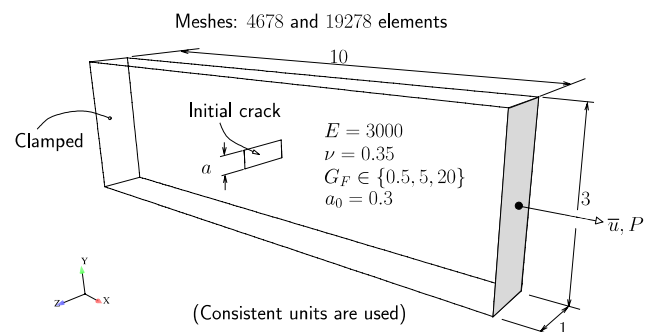


**Fig. 5** Pulling test: geometry, boundary conditions and material properties

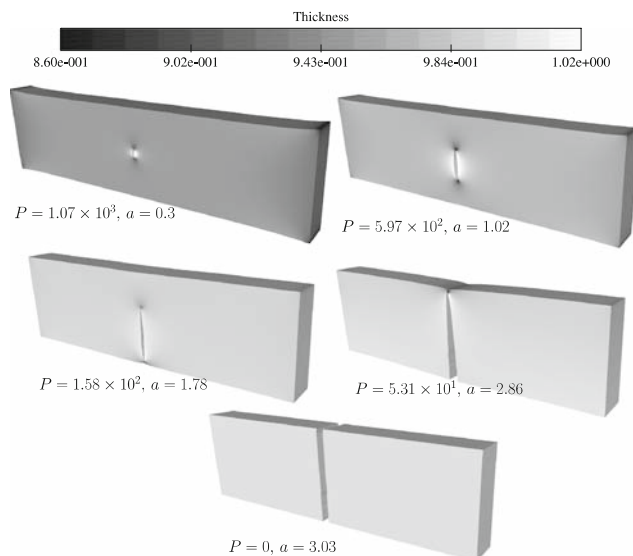


**Fig. 6** Pulling test: thickness contour plots for  $G_F = 20$  consistent units. The true deformed geometry is shown

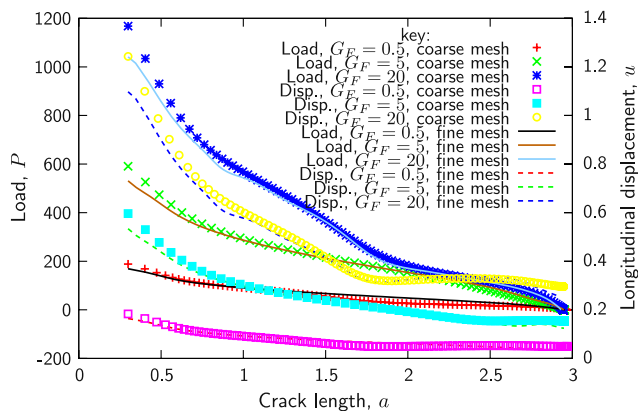


**Fig. 7** Pulling test: evolution of  $u$  and  $P$  with the crack length  $a$

tried a wide variety of step increments, stress-intensity factor criteria and crack path criteria.

In contrast, the problem is run without user-defined parameters, albeit a relatively fine mesh was also adopted near the holes for perfect fit. Only specimen #1 required smaller elements (which was also a conclusion of Bittencourt et al.) in the crack turning region near the second hole, but we use approximately the same mesh size for both specimens. The presence of the three holes perturbs the stress fields making the crack trajectory very sensitive to the position and size of the existent notch. The crack path in the absence of holes can be seen in Fig. 9 where it is marked as “pristine specimen” for both specimens. Despite previous well known accuracy difficulties (documented in [12] and implicitly seen in [30] who omit the crack turn), excellent agreement was observed between predicted and experimental crack paths (see Fig. 9). To the Authors’ knowledge, this accuracy was not achieved before by simulations.

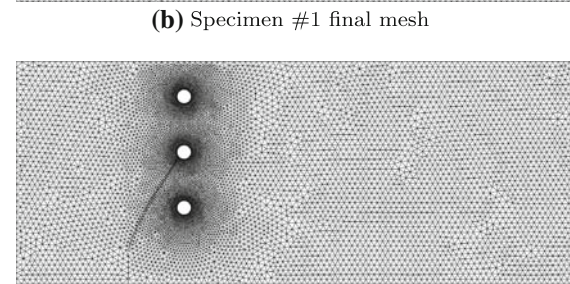
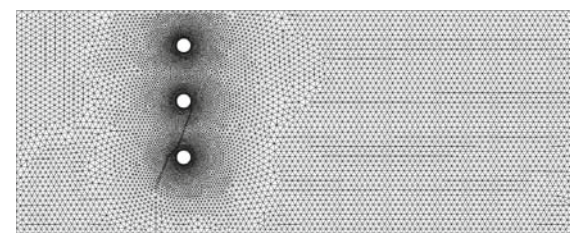
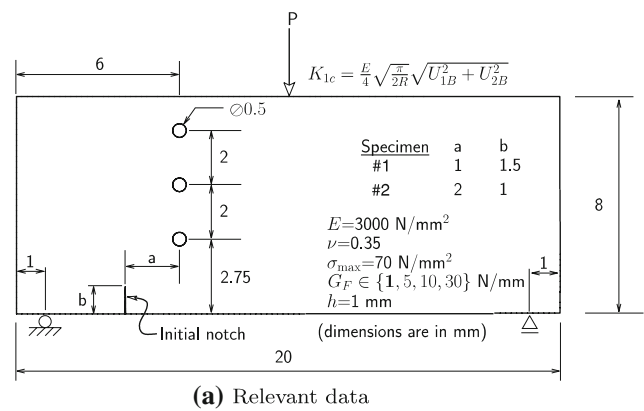


**Fig. 8** Bittencourt’s drilled plate: geometry, boundary conditions and material properties. Geometry parameters  $a$  and  $b$  vary according to the specimen. For specimen #1 we use a converged mesh of 17,782 elements and for specimen #2 we use a mesh of 17,932 elements. The two meshes after crack propagation are shown for  $G_F = 1$  N/mm

The crack mouth opening displacement (CMOD) is used to control the solution and capture the snap-backs. The principal stress contour plot is shown in Fig. 10 for both specimens over the true deformed mesh. Load-deflection and load-CMOD results are shown in Figs. 11 for specimen #1 and 12 for specimen #2. Very smooth results are obtained and we reach small energies without convergence problems. Sharper snap-backs may result in convergence difficulties. Accurate solution of more extreme situations requires the use of the so-called set-valued forces (see, e.g. [22]).

#### 4.3 Single edge notched beam

A simulation of the single edge notched (SEN) beam tested by Schlangen (cf. [39]) is performed. A geometrical description of this problem, with material properties and boundary conditions is shown in Fig. 13. Three uniform meshes are



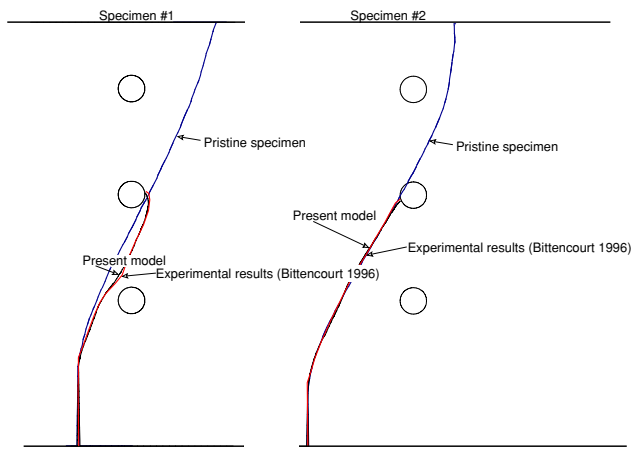


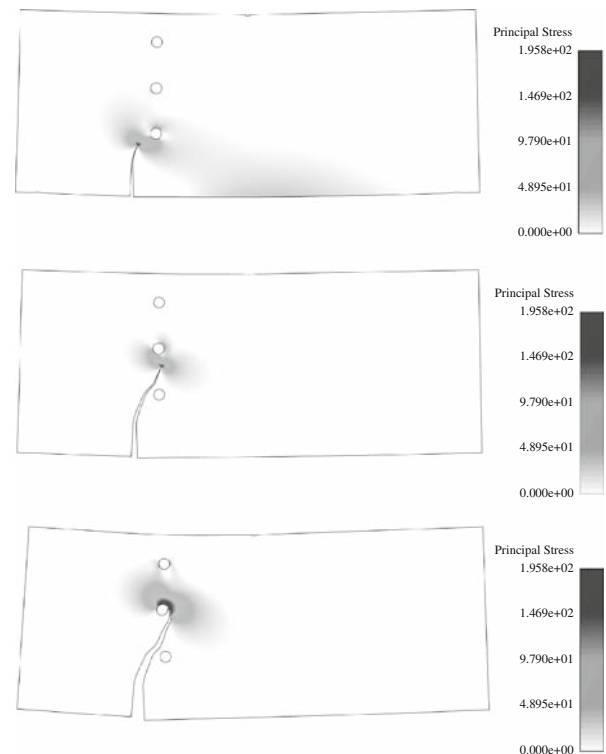
**Fig. 9** Bittencourt's drilled plate: comparison between experimentally obtained (cf. [12] in red here) and the present model with  $G_F = 1 \text{ N/mm.}$ , for specimens #1 and #2. Also shown in blue are the crack paths when holes are absent. Both geometries are undeformed

adopted, containing 4,532, 8,910 and 18,820 elements. The arc-length method (see Sect. 3.4) is used, with monotonically increasing CMSD (crack mouth sliding displacement). The crack path reproduces closely the experimental envelope, as can be observed in Fig. 14; even near the support the experimental observations are accurately reproduced.

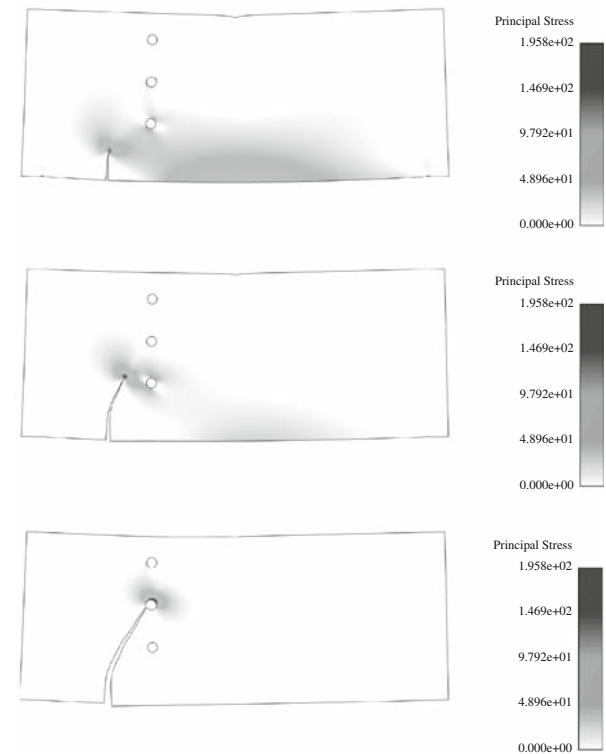
A comparison with the experimental results and the DSDA method [1,6,18], along with a study of mesh and step size influence is effected. As can be observed in Fig. 15, after the peak load is reached, the numerical results are more brittle than the experimental results. According to [2], this is due to the fact that an isotropic mode-I traction-jump law is used. The results are immune to the step-size up to very large CMSD increments.

#### 4.4 Cohesive crack growth in a four-point bending concrete beam

This problem consists of a bi-notched concrete beam subjected to two point loads. It was proposed by Bocca et al. [13] and numerically studied by a plethora of Authors. In the experimental setting and relevant data are described. From the set of specimens under inspection by Bocca et al. [13], we only retain specimens with  $c/b = 0.8$ ,  $b = 50$  and  $b = 200$  mm, since experimental load-displacement results are only available for these two cases. In addition to these results, we are also concerned with the crack paths that were reported in [13]. Using the well-known cracking particle method, Rabczuk and Belytschko [36] obtained very good results for the crack path in this problem, although the load in the load-displacement diagram was slightly higher than the experimental one. In addition, with the particle methods, there is the problem of choosing the support size in the crack region, which is not trivial. Our method does not consider



**(a)** Specimen #1 (not magnified),  $\bar{v} = \{0.277, 0.238, 0.186\}$



**(b)** Specimen #2 (not magnified),  $\bar{v} = \{0.433, 0.232, 0.218\}$

**Fig. 10** Bittencourt's drilled plate: sequence of contour plots over deformed meshes for both specimens,  $G_F = 1 \text{ N/mm}$ ;  $\bar{v}$  is the downward displacement of the loaded point

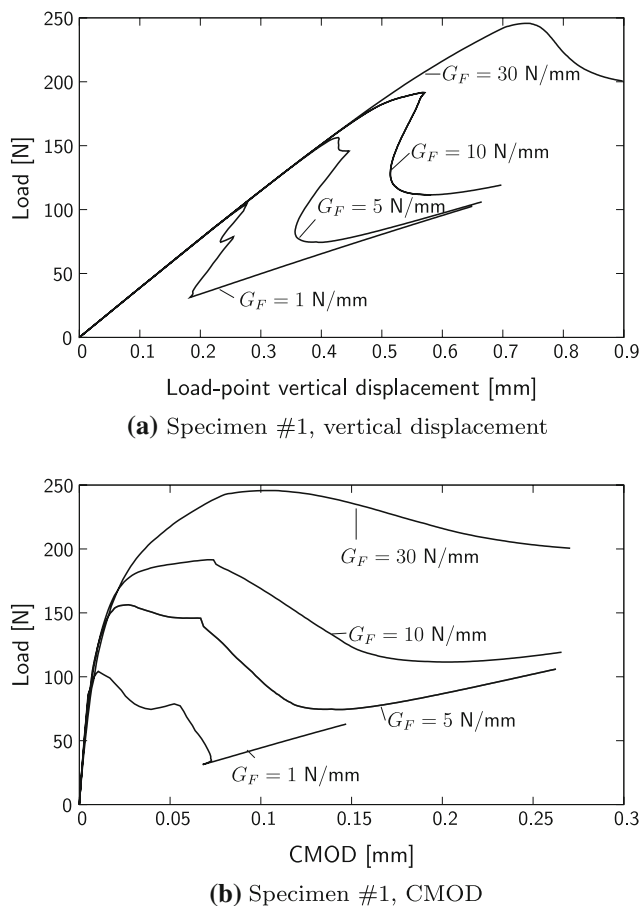


**Fig. 11** Bittencourt's drilled plate: specimen #1 load-vertical displacement and load-CMOD results for the loaded point for four values of  $G_F$

user-defined parameters besides mesh size. We use a single uniform mesh, with 19,860 initial elements. The relevant data is shown in Fig. 16. For anti-symmetry reasons, we impose the same mouth opening at the edge of notches A and B:  $\Delta u_B = \Delta u_A$ . It has been debated if quasi-static simulations allow propagation of more than one crack; we avoid this discussion here but note that many large research groups show this, (see the excellent thesis by Chaves [15]).

Two simultaneously evolving cracks occur and the result is typically sensitive to the mesh orientation and quality. We obtain an excellent agreement with the experimental crack paths, as shown in Fig. 17. The relatively wide spread of experimental crack paths is typical and results from the use of 6 specimens. Experimentally, some residual crack evolution in the opposite direction of the final path was observed and we also obtained that effect.

Load-displacement results are shown in Fig. 18 where a comparison with the measurements of Bocca et al. [13] and the cracking particle method of Rabczuk and Belytschko [36] is made. For the smaller specimen there is a slightly longer and lower curve than the observed one, but this is still

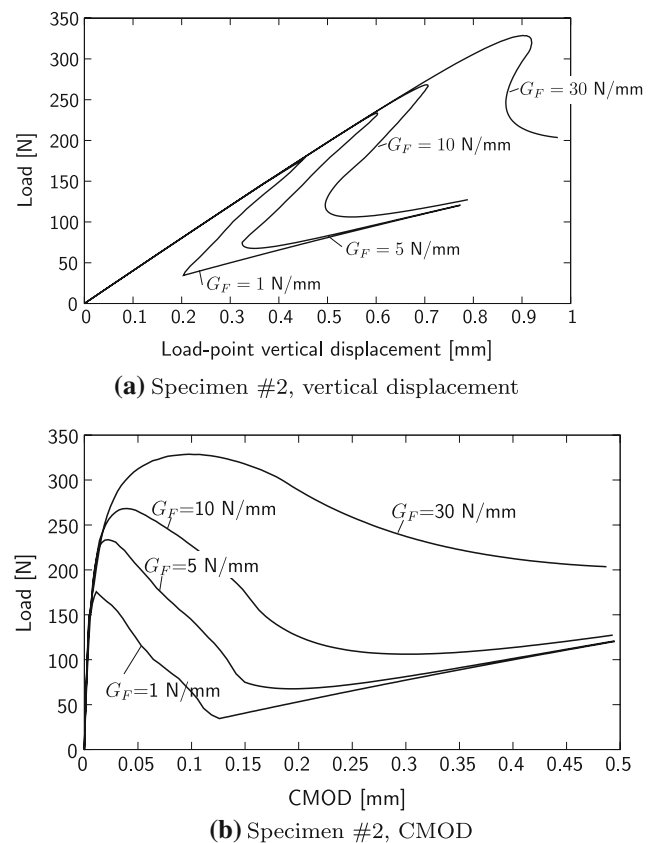


**Fig. 12** Bittencourt's drilled plate: specimen #2 load-vertical displacement and load-CMOD results for the loaded point for four values of  $G_F$

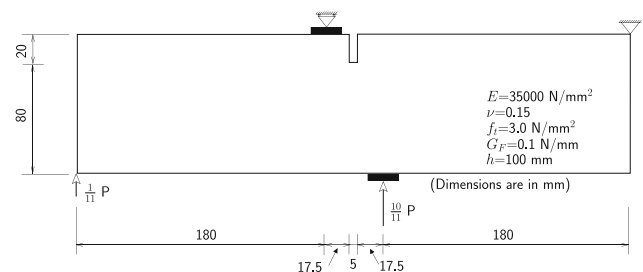


**Fig. 13** Schlagen's SEN test: geometry, boundary conditions and material properties

reasonable since the exact cohesive properties and the mode II effect are not accurately known.

The evolution of the angle error ( $\varepsilon_\alpha$ ) with the number of steps is shown in Fig. 19 for both cases (with and without mesh repositioning). The well known crack back-turning phenomenon occurs in the latter case; the detail in this figure shows this effect in the upper crack. The analysis was halted at this point.

The effect of step size in the convergence behavior is shown in Fig. 20 for the first 100 iterations. Quadratic convergence is observed despite some error growth in early iterations for  $\Delta \text{CMSD} = 2 \times 10^{-3} \text{ mm}$ .

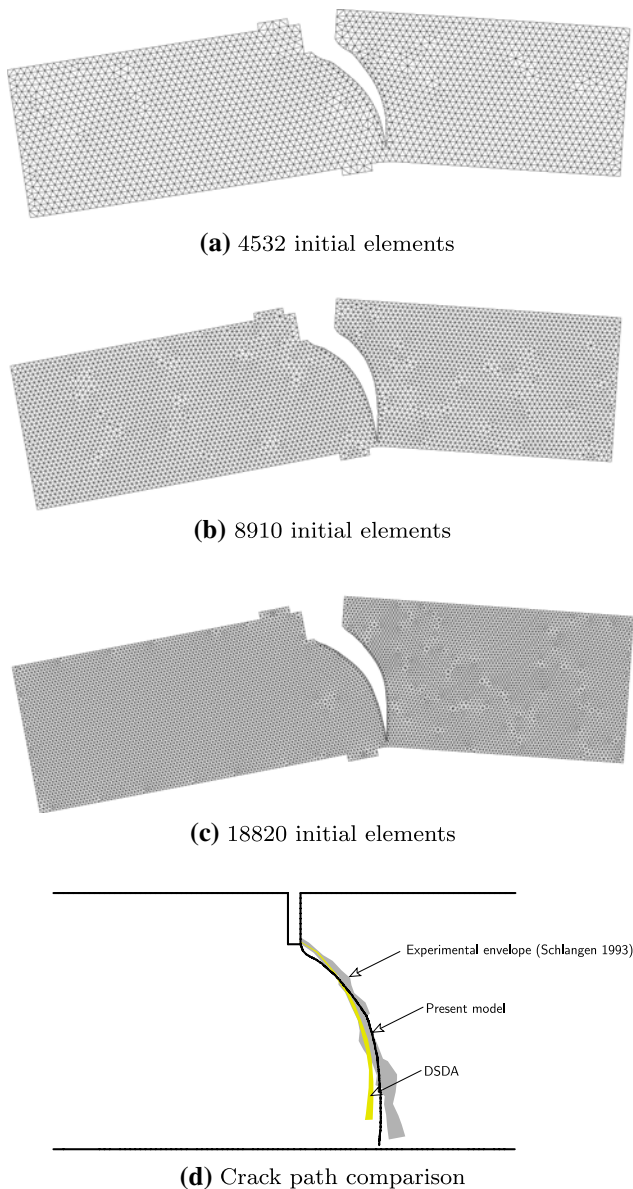


**Fig. 14** Schlangen's SEN test: Deformed meshes for the 3 cases are shown, with 4,532, 8,910 and 18,820 elements and  $\text{CMSD} = 0.1$  mm. Crack path (8,910 initial elements) compared with DSDA [18] (yellow) and the experimental results by Schlangen [39]

#### 4.5 Simultaneous propagation of 10 cracks under normal and shear strain

In this problem we analyze a square, plane-strain, plate containing 10 cracks. It is a variation of the test by Zi et al. [44] who performed a fatigue cycle counting with the same geometry and crack arrangement. The tests involve multiple crack growth and coalescence including intersections with the outer boundary. The problem data and the crack positioning are shown in Fig. 21. As can be observed, two meshes are used for comparison. Essential boundary conditions are slightly

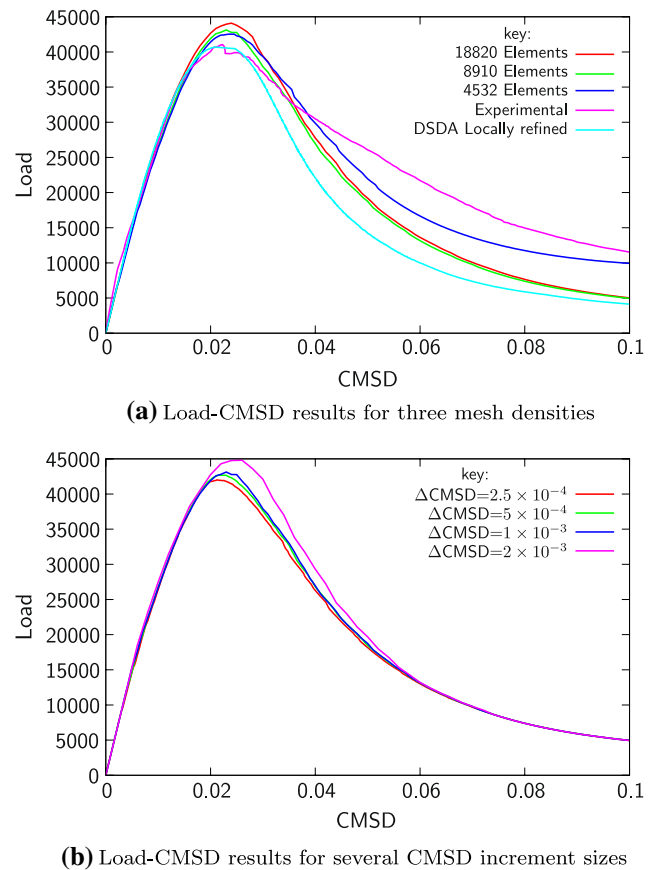


**Fig. 15** Schlangen's SEN test: load-CMSD results: comparison with the experimental results by Schlangen [39], the DSDA technique and effect of mesh and step size

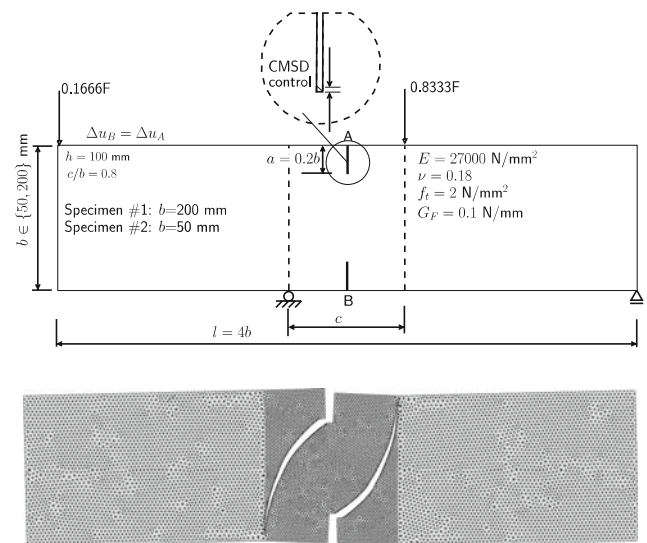


**Fig. 16** Four-point bending of a concrete beam: geometry, boundary conditions, multipoint constraints ( $\Delta u_B = \Delta u_A$ ) and material properties. Also shown is the final deformed mesh 10× magnified

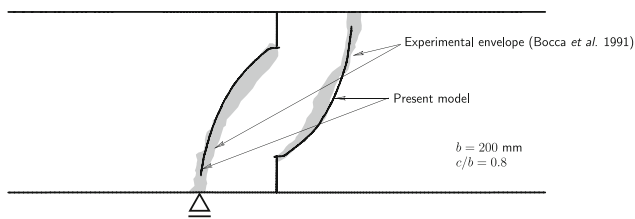


**Fig. 17** Four-point bending of a concrete beam: crack paths compared with the envelope of experimental results by Bocca et al. [13]

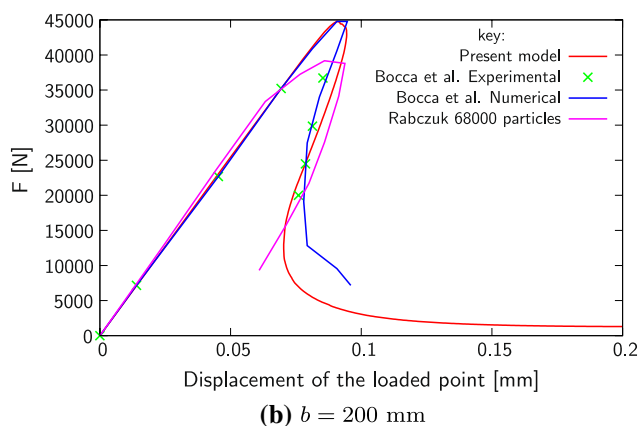
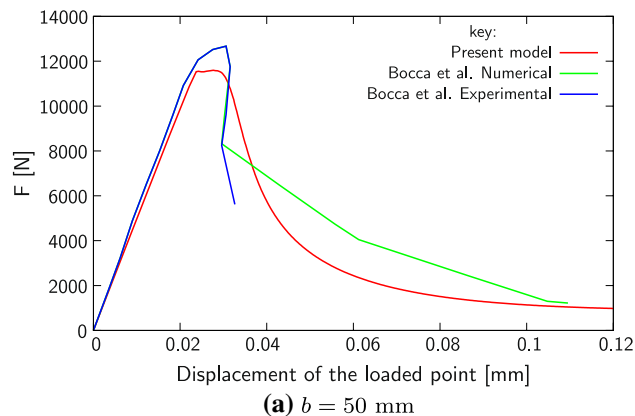


**Fig. 18** Load-displacement results, compared with the results of Bocca et al. [13] and the cracking particle method of Rabczuk and Belytschko [36] (for the case  $b = 200$  mm) with their 68,000 particle analysis

different than what was reported in [44], since only limited crack extension was obtained by those Authors. Additionally, two load cases are inspected here.

Deformed mesh sequences (using the finer mesh) for case A can be seen in Fig. 22. The homogenized Kirchhoff stress versus the Hencky strain are depicted in Fig. 23. It can be observed that, despite the large difference in mesh density (the ratio of  $h_c$ , with  $h_c$  being the characteristic element size, is around 1.66), a close reproduction of results is obtained. This also indicates that the growth is immune to spurious crack shielding. All cracks can grow simultaneously until their length fails to satisfy the critical stress intensity factor

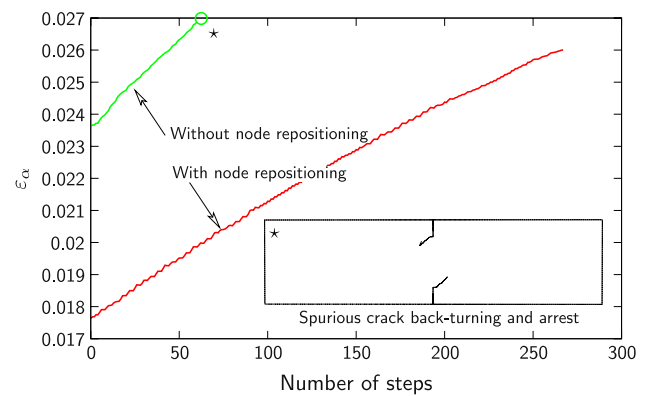


**Fig. 19** Evolution of the angle error ( $\varepsilon_\alpha$ ) with the number of time steps

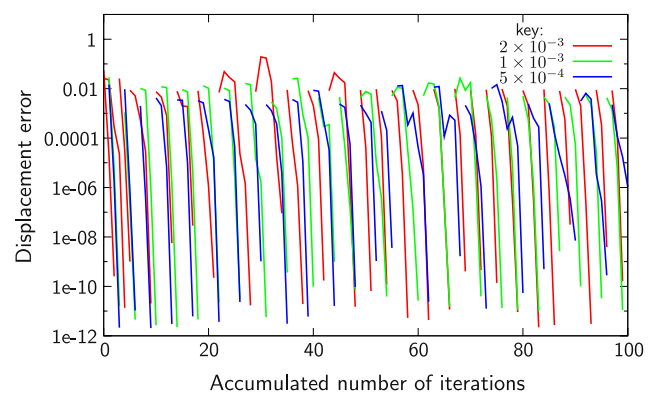


**Fig. 20** Displacement error for the first 100 accumulated iterations for  $\Delta\text{CMSD} = 2 \times 10^{-3}$ ,  $1 \times 10^{-3}$  and  $\Delta\text{CMSD} = 5 \times 10^{-4}$

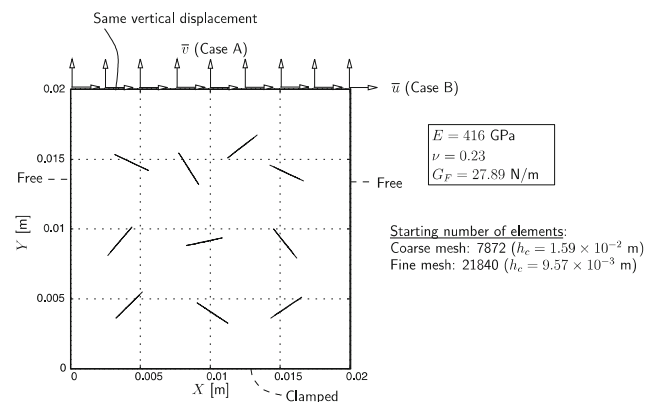


**Fig. 21** Multiple crack test: problem data, geometry and material properties (adapted from [44])

criterion. The reader can also verify that, even taking in consideration the different analysis type, our methodology leads to more realistic behavior than the one shown in [44].

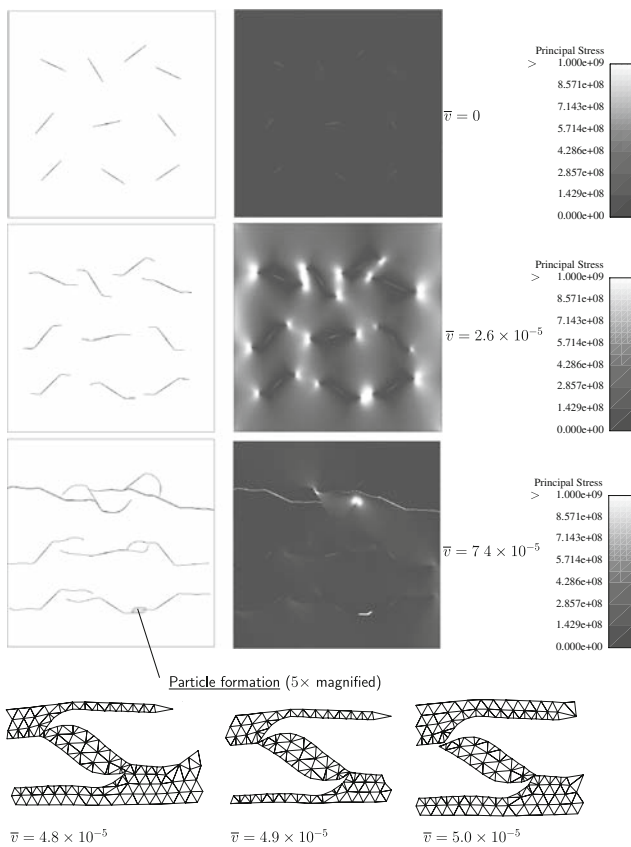


**Fig. 22** Multiple crack test: sequence of deformed meshes illustrating growth, coalescence and intersection of cracks for the fine mesh (see Fig. 21) for the load case A. Principal stress  $\tau_1$  grayscale contour plots are also shown. In detail, we can observe the formation of a particle by simultaneous crack growth

#### 4.6 Nooru's mixed-mode panel

A double-edge notched specimen is subject to mixed-mode inducing loads. This experiment was proposed and studied by Nooru–Mohamed [33]; the  $200 \times 200 \times 50$  mm specimen has two  $25 \times 5$  mm horizontal notches located at half-height as shown in Fig. 24. Two L-shaped steel frames are glued to the specimen and the loading is applied at the top steel frame. One of the experimental load paths is numerically simulated: first, a horizontal force  $P_h$  is progressively applied until the value  $P_{\max}$  is reached. Then, the force is kept constant and a vertical displacement  $v$  is gradually applied (see Fig. 24). The material parameters are also taken from [33].

Two unstructured meshes are tested: a coarse mesh with 2,326 triangular elements and a fine mesh with 5,278 triangular elements. Two values of  $P_{\max}$  are used: 5 and 10 kN. The two crack paths are shown in Fig. 25 where the experimental results from [33] are superimposed. Also shown, for the case  $P_{\max} = 10$  kN, is the crack path obtained with the DSDA method (see references [1, 6]). The crack paths agree reasonably, although not perfectly, with the experimental results.

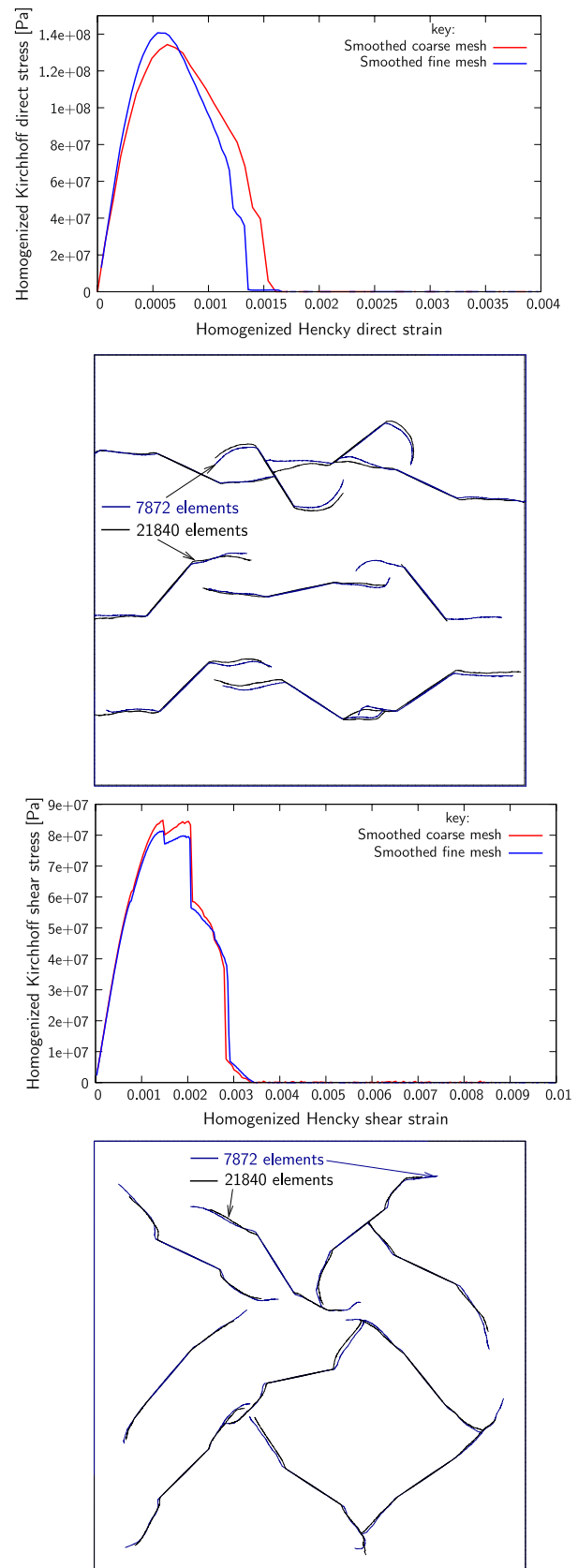


**Fig. 23** Homogenized stress-strain results for both meshes (load cases A and B) and comparison between crack paths for the two initial meshes



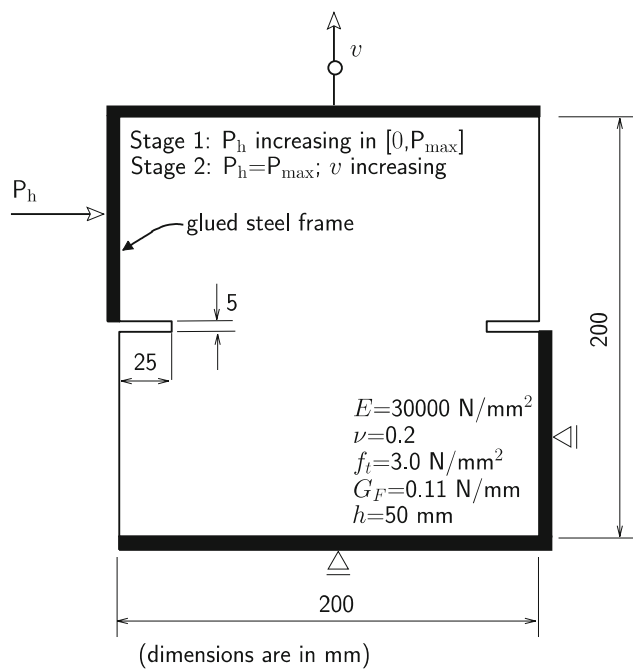


**Fig. 24** Nooru's mixed-mode panel: problem data, geometry, boundary conditions and material properties

However, we must remark that there is considerable scatter in the latter.

## 5 Conclusions and outlook

A simple method to solve brittle and quasi-brittle crack propagation 2D problems was described and tested; observed effects in experiments such as intersection, coalescence and particle formation were successfully obtained. This is not easily done with enrichment methods (see [5–8]). A combination of local tip remeshing, recursive subdivision and nodal repositioning was proposed which solves well-known issues in crack modeling with traditional enrichment or remeshing methods:

- Difficulties in modeling crack intersection and coalescence
- Crack tip and step size dependence
- Presence of blade and dagger-shaped finite elements
- Representation of thickness variation at the crack faces due to plane stress condition or incompressibility.

Excellent crack path agreement with experiments was systematically obtained. Good load-deflection and load-CMOD results were also observed. Quadratic convergence was always achieved in problems where the cohesive law was used. In all examples both step size and mesh near-independence was observed and, after solving the aforementioned

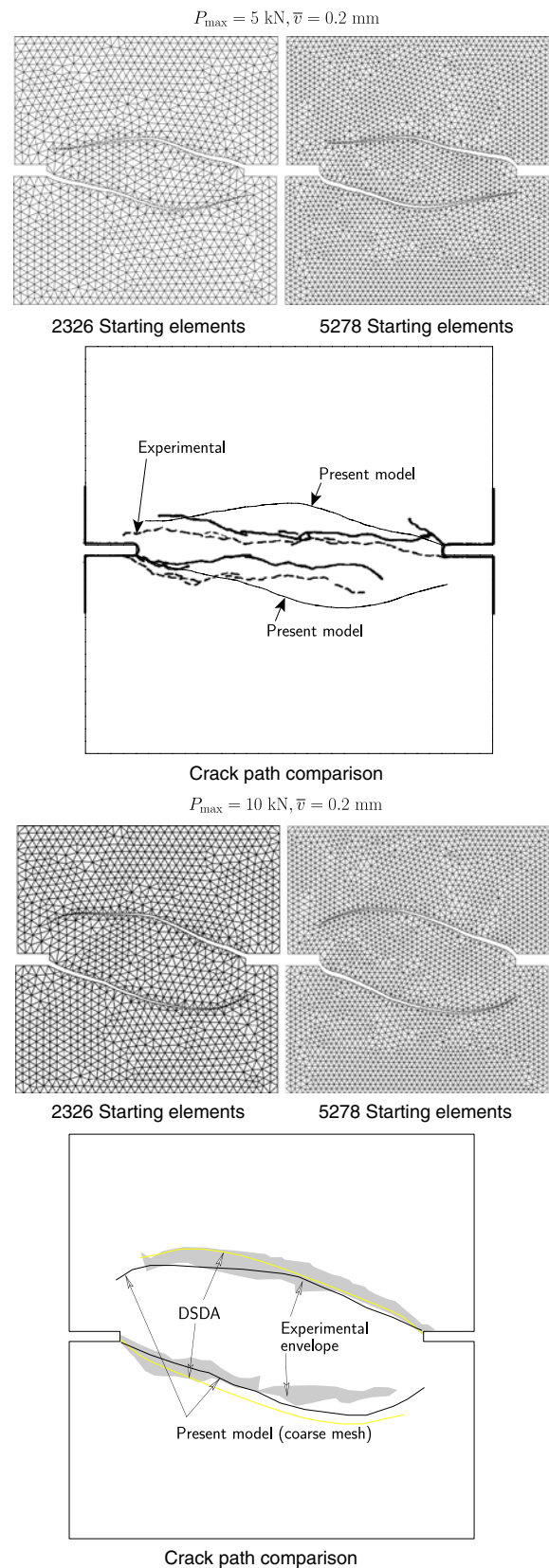


**Fig. 25** Nooru's mixed-mode panel: crack path comparisons for  $F = 5$  kN and  $F = 10$  kN. The experimental envelope and the DSDA results are shown for  $P_{\max} = 10$  kN

problems, we found the present framework robust enough to be used as one scale in a multiscale simulation.

Perspectives of application to finite strain plasticity can make use of the strong ellipticity condition and continuum-based cohesive laws.

## References

- Alfaia J, Simone A, Sluys LJ (2003) A new approach to strong embedded discontinuities. In: Bicanic N, de Borst R, Mang H, Meschke G (eds) Computational modelling of concrete structures, EURO-C 2003. St. Johann im Pongau, Salzburger Land, Austria
- Alfaia J, Wells GN, Sluys LJ (2002) On the use of embedded discontinuity elements with crack path continuity for mode-I and mixed-mode fracture. *Eng Fract Mech* 69:661–686
- Antman SS (2005) Nonlinear problems of elasticity, 2nd edn. Springer, Heidelberg
- Areias P. Simplas. <https://ssm7.ae.uiuc.edu:80/simplas>
- Areias PMA, Belytschko T (2005) Analysis of three-dimensional crack initiation and propagation using the extended finite element method. *Int J Numer Meth Eng* 63:760–788
- Areias PMA, César de Sá JMA, Conceição António CA, Carneiro JASAO, Teixeira VMP (2004) Strong displacement discontinuities and Lagrange multipliers in the analysis of finite displacement fracture problems. *Comput Mech* 35:54–71
- Areias PMA, Rabczuk T (2008) Quasi-static crack propagation in plane and plate structures using set-valued traction-separation laws. *Int J Numer Meth Eng* 74:475–505
- Areias PMA, Song JH, Belytschko T (2006) Analysis of fracture in thin shells by overlapping paired elements. *Comp Method Appl M* 195(41–43):5343–5360
- Askas H, Kuhl E, Steinmann P (2004) ALE formulation based on spatial and material settings of continuum mechanics. *Comp Method Appl M* 193:4223–4245
- Bažant ZP, Planas J (1998) Fracture and size effect in concrete and other quasibrittle materials. CRC Press, Boca Raton
- Belytschko T, Black T (1999) Elastic crack growth in finite elements with minimal remeshing. *Int J Numer Meth Eng* 45:601–620
- Bittencourt TN, Ingraffea AR, Wawrzynek PA, Sousa JL (1996) Quasi-automatic simulation of crack propagation for 2D LEFM problems. *Eng Fract Mech* 55(2):321–334
- Bocca P, Carpinteri A, Valente S (1991) Mixed mode fracture of concrete. *Int J Solids Struct* 27(9):1139–1153
- Bonet J, Wood RD (1997) Nonlinear continuum mechanics for finite element analysis. Cambridge University Press, London
- Chaves EWV (2003) PhD thesis, Universitat Politècnica de Catalunya, Escola Tècnica Superior D'Enginyers de Camins, Canals I Ports. Barcelona, Spain
- Colombo D, Giglio M (2006) A methodology for automatic crack propagation modelling in planar and shell fe models. *Eng Fract Mech* 73:490–504
- Crisfield MA (1997) Non-linear finite element analysis of solids and structures, vol 2. Wiley, London
- Dias-da-Costa D, Alfaia J, Sluys LJ, Júlio E (2009) A discrete strong discontinuity approach. *Eng Fract Mech* 76(9):1176–1201
- Elices M, Guinea GV, Gómez J, Planas J (2002) The cohesive zone model: advantages, limitations and challenges. *Eng Fract Mech* 69:137–163
- Erdogan F, Sih GC (1963) On the crack extension in plates under plane loading and transverse shear. *J Bas Eng* 85:519–527
- Etse G, Willam K (1999) Failure analysis of elastoviscoplastic material models. *J Eng Mech-ASCE* 125:60–69
- Glocker C (2001) Set-valued force laws, dynamics of non-smooth systems. Lecture notes in applied mechanics, vol 1. Springer, Berlin
- Hallquist JO (2006) LS-DYNA theory manual. Livermore software technology corporation. Livermore, California
- Hansbo A, Hansbo P (2004) A finite element method for the simulation of strong and weak discontinuities in solid mechanics. *Comp Method Appl M* 193:3523–3540
- Hughes TJR (1987) The finite element method, Linear static and dynamic finite element analyses. Prentice-Hall, Englewood Cliffs, NJ
- Karihaloo BL, Xiao QZ (2003) Modelling of stationary and growing cracks in FE framework without remeshing: a state-of-the-art review. *Comput Struct* 81:119–129
- Legrain G, Moës N, Verron E (2005) Stress analysis around crack tips in finite strain problems using the extended finite element method. *Int J Numer Meth Eng* 63:290–314
- Loehnert S, Belytschko T (2007) A multiscale projection method for macro/microcrack simulations. *Int J Numer Meth Eng* 71:1466–1482
- Ma F, Deng X, Sutton MA, Jr, Newman JC (1999) Mixed-mode crack behavior, chapter A CTOD-based mixed-mode fracture criterion. Number STP 1359. ASTM American Society for Testing and Materials, West Conshohocken, PA, pp 86–110
- Miehe C, Gürses E (2007) A robust algorithm for configurational force-driven brittle crack propagation with  $r$ -adaptive mesh alignment. *Int J Numer Meth Eng* 72:127–155
- Moës N, Belytschko T (2002) Extended finite element method for cohesive crack growth. *Eng Fract Mech* 69:813–833
- Moës N, Dolbow J, Belytschko T (1999) A finite element method for crack growth without remeshing. *Int J Numer Meth Eng* 46:131–150
- Nooru-Mohamed MB (1992) Mixed-mode fracture of concrete: an experimental approach. PhD thesis, Delft University of Technology, The Netherlands
- Oliver J (1989) A consistent characteristic length for smeared cracking models. *Int J Numer Meth Eng* 28:461–474
- Oliver J (1995) Continuum modelling of strong discontinuities in solid mechanics using damage models. *Comput Mech* 17:49–61
- Rabczuk T, Belytschko T (2004) Cracking particles: a simplified meshfree method for arbitrary evolving cracks. *Int J Numer Meth Eng* 61:2316–2343
- Rodríguez-Ferran A, Casadei F, Huerta A (1998) ALE stress update for transient and quasistatic processes. *Int J Numer Meth Eng* 43:241–262
- Rodríguez-Ferran A, Pérez-Foguet A, Huerta A (2002) Arbitrary lagrangian-eulerian (ALE) formulation for hyperelastoplasticity. *Int J Numer Meth Eng* 53:1831–1851
- Schlangen E (1993) Experimental and numerical analysis of fracture processes in concrete. PhD thesis, Delft
- Schreyer HL, Chen Z (1986) One-dimensional softening with localization. *J Appl Mech-ASME* 53:791–797
- Teng X, Wierzbicki T (2006) Evaluation of six fracture models in high velocity perforation. *Eng Fract Mech* 73:1653–1678
- Wolfram Research Inc. (2008) Mathematica, version 7.0, Champaign, IL
- Xu H, Newman TS (2006) An angle-based optimization approach for 2d finite element mesh smoothing. *Finite Elem Anal Des* 42:1150–1164
- Zi G, Song J-H, Budyn E, Lee S-H, Belytschko T (2004) A method for growing multiple cracks without remeshing and its application to fatigue crack growth. *Model Simul Mater Sc* 12:901–915